Progress In Electromagnetics Research C, Vol. 104, 187–199, 2020

Free Vibration of Magnetic Gear with Intersecting Axes

Xiuhong Hao, Wenbin Hao, Qingkan Wang, and Deng Pan*

Abstract—The dynamic performance optimization of magnetic gear devices is essential to their industrialization. In this study, upon considering the magnetic field coupling characteristics of different components of a field modulated magnetic gear with intersecting axes (FMMGIA), we first obtained the magnetic coupling stiffnesses of these components via the finite element method. On this basis, we further established a dynamic model as well as the corresponding differential equations for the magnetic gear. Thereafter, we analyzed the modal characteristics and the influences of the primary design parameters on the modal frequency of the FMMGIA system. The results indicated that the magnetic coupling stiffnesses among the FMMGIA components were significantly lower than the meshing stiffnesses of the mechanical gears. In addition, the magnetic gear system consisted of three orders of torsional modals as well as three orders of horizontal vibration modals, among which the torsional modal frequencies of both the input and output rotors were substantially lower than others. Finally, parameters such as the minimum axial length and the permanent magnet remanence demonstrated considerable have impacts on the modal frequencies of the FMMGIA system.

1. INTRODUCTION

The magnetic gear transmission system is capable of motion and power transmission through magnetic field coupling, featuring advantages including no contact, no wear, no lubrication, and overload protection. This system overcomes the mechanical gear drawback of gear teeth breakage due to contact fatigue, making it one of the best alternatives to mechanical gear transmission [1].

Compared to conventional magnetic gears with parallel axes that adopt the topological structure of mechanical gears, the field modulated magnetic gear (FMMG) presents advantages including efficient utilization of permanent magnets (PMs) and large output torque. The higher torque density of the FMMG is up to $147\,\mathrm{kN\cdot m/m^3}$, and transmission capacity is comparable to that of the mechanical gear [2, 3]. Thus, over the past two decades, the FMMG has attracted substantial attention from various industries, resulting in emerging research achievements such as novel magnetic gear devices and integrated motors [4, 5]. However, despite a large number of in-depth investigations on transmission mechanism [6], transmission efficiency [7], parameter optimization [8], component deformation, etc. [9] of these devices and integrated motors, relatively few studies exist on the dynamics of the magnetic gear [10]. Studies by Hao et al. and Montague et al. indicated that the magnetic coupling stiffnesses of the components of a magnetic gear system were much smaller than the meshing stiffnesses of the mechanical gears [10, 12], resulting in slower transient resonant attenuation of the system upon certain excitation, which aggravated the dynamic behavior of the system to a certain extent. Frank et al. inserted damping coils into the rotor to increase the electromagnetic damping and consequently accelerate the vibrational attenuation of the components. However, their study failed to address the decrease in the output torque and transmission efficiency of the system [11]. As the service indicators of motion and power transmission devices rely heavily on their dynamic performance, their optimization is essential to the

---

Received 15 January 2020, Accepted 24 April 2020, Scheduled 14 August 2020

* Corresponding author: Deng Pan (pandeng1896@sina.com).

The authors are with the School of Mechanical Engineering, Yanshan University, Hebei 066004, China.

industrialization of these devices. Compared with mechanical gears, the dynamic characteristics of magnetic gears are poor. Especially, when the output torque suddenly increases and does not exceed the maximum output torque, there are larger overshoot and longer transient time from one steady running state to another steady running state [13].

The most suitable design for the magnetic field modulation mechanism of the magnetic gear is a coaxial structure, which also facilitates integration with motors [14]. Therefore, other types of implementations, such as the field modulated magnetic gears with the intersecting axes (FMMGIA), have received significantly less attention, although they have higher output torque and torque density than the traditional intersecting shaft magnetic gears and are equally important as an alternative to mechanical bevel gears [15, 16]. Based on our previous work on transmission mechanisms and structural optimization, we established a three-dimensional dynamic model and the corresponding differential equations of the magnetic gear system, analyzed the modal characteristics of the system, and identified the effects of different design parameters on the modal frequency. This work provides a theoretical basis for the structural optimization and dynamic performance enhancement of the FMMGIA.

2. DYNAMIC MODEL AND DIFFERENTIAL EQUATION SET

Figure 1 shows the structure of the FMMGIA, which mainly consists of ferromagnetic pole-pieces (FP), an input rotor, and an output rotor. Both the input and output rotors are composed of a back iron and PMs, which are magnetized via axial magnetization so that N-poles and S-poles are layered at regular intervals on the back iron. The linear FP is composed of permeable and non-permeable magnetic strips at alternating intervals that form an elliptical cross section, and the two end-faces of the pole pieces opposite to the PMs have a ring-shape and an intersection angle of 90°. By changing this angle or the cross-sectional shape of the FP, the intersection angle between the input and output shafts can be tailored. An air gap also exists between the input/output rotors and the two end-faces of the pole pieces. The primary function of the FP is to regulate the main harmonics in the air gap at each of the two sides so as to achieve equal magnetic pole coupling of the magnetic gear, thereby generating motion and power.

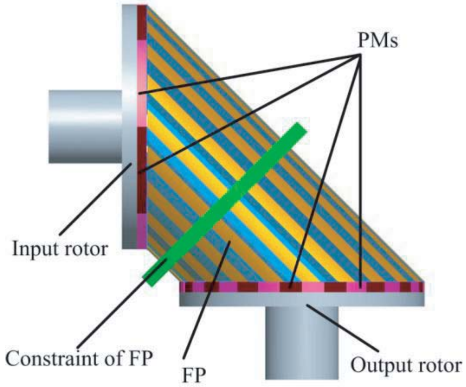

Figure 1. Structure of the FMMGIA.

2.1. Dynamic Model and Differential Equation Set

The dynamic model of the FMMGIA system consists of models for two subsystems, i.e., the input rotor/FP subsystem and FP/output rotor subsystem. The dynamic models of the two subsystems are established individually; then, the dynamic model of the entire transmission system can be established by combining them. When establishing the dynamic model, the following assumptions are made based on the actual structure of the system:

(1) The main components are rigid; in particular, the PM and the back iron form an integrated rigid body without internal sliding. Subtle elastic deformations of the components are ignored during

the transmission process.

(2) Only the rotational vibration of the components and their lateral vibrations on the rotational plane are considered, whereas vibrations at other degrees of freedom are ignored.

(3) The friction between moving components as well as the time-varying portion of the magnetic coupling stiffnesses due to magnetic field modulation are ignored.

(4) The magnetic couplings between the PMs and FP on both the input and output rotors are simplified as linear springs along the tangential and lateral directions. In addition, the support between the input/output rotors and the substrate can also be represented by a linear spring along the lateral direction. Lastly, the constraint between the FP and the substrate can be simplified as linear spring constraints along the tangential and lateral directions.

(5) The system does not experience issues such as desynchronizing due to overload.

(6) The manufacturing and assembling errors of all components are ignored. The PMs on the input and output rotors are assumed to have identical sizes and performance parameters, so are the permeable and non-permeable parts of the FP.

(7) The effects of eddy-current loss among the components of the FMMGIA system on the magnetic coupling stiffness are ignored.

(8) Fluctuations in the input and output loads may cause low-frequency or high-frequency resonance but will not change the modal characteristics of the FMMGIA system.

The resultant dynamic model of the magnetic gear system based on the spatial structure and the established dynamic assumptions are shown in Fig. 2. Subsequently, the dynamic equations of the two subsystems were established individually and then combined to derive the equation of the overall transmission system.

When establishing the dynamic model of the FMMGIA system, to simplify calculations, the torsional angular displacements θ_I, θ_s, and θ_o of the input rotor, FP, and output rotor, respectively,

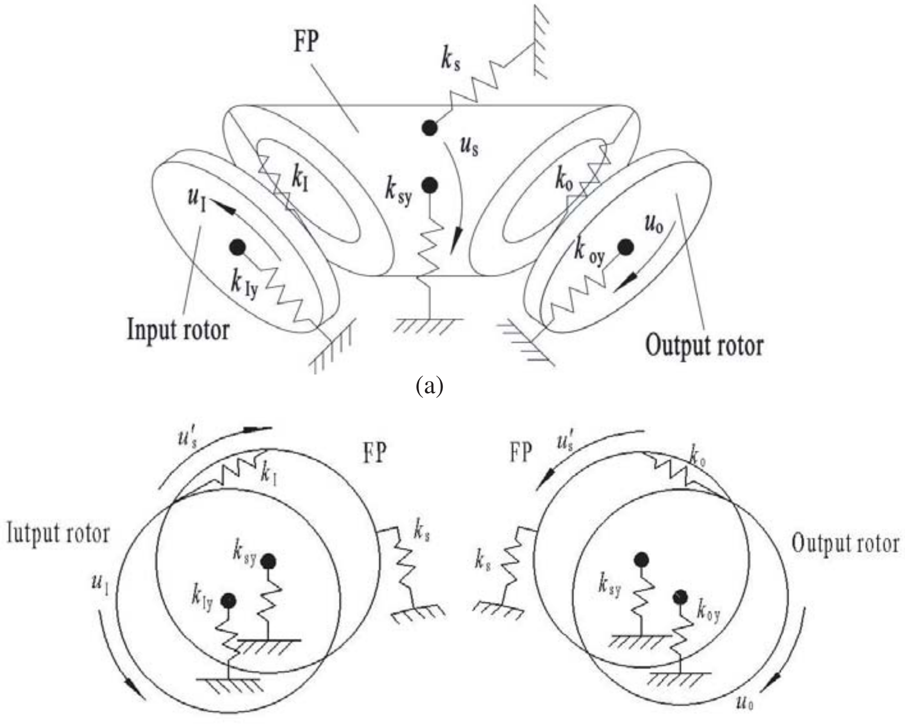

(a)

(b) (c)

Figure 2. Dynamic model of the entire transmission system: (a) The dynamic models; (b) The input rotor/FP subsystem; (c) The FP/output rotor subsystem.

were replaced with the corresponding torsional linear displacements u_I, u_s, and u_o, i.e.,

$$u_i = R_i\theta_i, \quad i = I, s, o \tag{1}$$

where R_I, R_s, and R_o denote the rotational radius of the input rotor, pole-pieces, and output rotor, respectively.

By representing the vibrational displacement of the input rotor, FP, and output rotor along the lateral support direction by y_I, y_s, and y_o, respectively, the displacements of the FMMGIA system at each degree of freedom can be expressed by the following matrix:

$$\boldsymbol{x} = [\ u_I \quad y_I \quad u_s \quad y_s \quad u_o \quad u_o\ ]^T \tag{2}$$

2.1.1. Input Rotor/FP Subsystem

The dynamic model of the input rotor/FP subsystem is shown in Fig. 2(a). The differential equations of the model can be expressed as follows:

$$\begin{cases} M_I\ddot{u}_I + k_I x_I \cos\beta_I = T_I/R_I \\ m_I\ddot{y}_I + k_I x_I \sin\beta_I + k_{Iy}y_I = 0 \\ M_s\ddot{u}_s \sin\varphi - k_I x_I \cos\beta_I + k_s u_s \sin\varphi = 0 \\ m_s\ddot{y}_s - k_I x_I \sin\beta_I \sin\varphi + k_{sy}y_s = 0 \end{cases} \tag{3}$$

where M_I and M_s are the equivalent masses (kg) of the input rotor and FP, respectively, when rotating about their axes, and $M_I = J_I/R_I^2$ and $M_s = J_s/R_s^2$, where J_I and J_s are the rotational inertia ($\mathrm{kg}\cdot\mathrm{m}^2$) of the input rotor and the FP when rotating along their axes, respectively; m_I and m_s are the masses (kg) of the input rotor and the FP, respectively; k_{Iy} and k_{sy} are the lateral support stiffnesses (N/m) of the input rotor and FP, respectively; k_s is the torsional support stiffness (N/m) of the FP; k_I is the magnetic coupling stiffness (N/m) between the input rotor and the FP, and $k_I = \sqrt{k_{Ir}^2 + k_{It}^2}$; k_{Ir} and k_{It} are the radial and tangential components (N/m) of the magnetic coupling stiffness between the input rotor and the FP, respectively; x_I is the relative displacement (m) between the input rotor and FP; β_I is the intersection angle (°) between the radial and tangential components of the magnetic coupling stiffness between the input rotor and FP, $\beta_I = \arctan(k_{Ir}/k_{It})$; φ is the intersection angle (°) between the end-face of the FP and central axis, and T_I is the fluctuation torque (N/m) on the input rotor.

The relative displacement x_I between the input rotor and the FP is given by

$$x_I = (u_I - u_s)\cos\beta_I + (y_I - y_s)\sin\beta_I \tag{4}$$

By substituting Equation (4) into the dynamic differential Equation (3), we get

$$\begin{cases} M_I\ddot{u}_I + k_I(u_I - u_s)\cos^2\beta_I + k_I(y_I - y_s)\sin\beta_I\cos\beta_I = T_I/R_I \\ m_I\ddot{y}_I + k_I(u_I - u_s)\sin\beta_I\cos\beta_I + k_I(y_I - y_s)\sin^2\beta_I + k_{Iy}y_I = 0 \\ M_s\ddot{u}_s\sin\varphi - k_I(u_I - u_s)\cos^2\beta_I - k_I(y_I - y_s)\sin\beta_I\cos\beta_I + k_s u_s\sin\varphi = 0 \\ m_s\ddot{y}_s - k_I(u_I - u_s)\sin\beta_I\cos\beta_I\sin\varphi - k_I(y_I - y_s)\sin^2\beta_I\sin\varphi + k_{sy}y_s = 0 \end{cases} \tag{5}$$

2.1.2. FP/output Rotor Subsystem

The dynamic model of the FP/output rotor subsystem is shown in Fig. 2(b). The differential equations of the model can be expressed as follows:

$$\begin{cases} M_s\ddot{u}_s\sin\varphi - k_o x_o\cos\beta_o + k_s u_s\sin\varphi = 0 \\ m_s\ddot{y}_s - k_o x_o\sin\beta_o\sin\varphi + k_{sy}y_s = 0 \\ M_o\ddot{u}_o + k_o x_o\cos\beta_o = T_o/R_o \\ m_o\ddot{y}_o + k_o x_o\sin\beta_o + k_{oy}y_o = 0 \end{cases} \tag{6}$$

where M_o is the equivalent mass (kg) of the output rotor when rotating along its axis $M_o = J_o/R_o^2$; J_o is the rotational inertial ($\mathrm{kg}\cdot\mathrm{m}^2$) of the output rotor when rotating along its axis; m_o is the mass (kg) of the output rotor; k_{oy} is the lateral support stiffness (N/m) of the output rotor; k_o is the magnetic coupling stiffness (N/m) between the output rotor and FP, and $k_o = \sqrt{k_{or}^2 + k_{ot}^2}$; k_{or} and k_{ot} are the radial and tangential components (N/m) of the magnetic coupling stiffness between the output rotor and the FP, respectively; x_o is the relative displacement (m) between the output rotor and the FP; β_o is the intersection angle (°) between the radial and the tangential components of the magnetic coupling stiffness between the output rotor and the FP, $\beta_o = \arctan(k_{or}/k_{ot})$, and T_o is the fluctuation torque (N/m) on the output rotor.

The relative displacement x_o between the output rotor and the FP can be calculated by

$$x_o = (u_o - u_s)\cos\beta_o + (y_o - y_s)\sin\beta_o \tag{7}$$

By substituting Equation (7) into the dynamic differential Equation (6), we then obtain the dynamic equation set for the FP/output rotor subsystem:

$$\begin{cases} M_s\ddot{u}_s\sin\varphi - k_o(u_o - u_s)\cos^2\beta_o - k_o(y_o - y_s)\sin\beta_o\cos\beta_o + k_s u_s\sin\varphi = 0 \\ m_s\ddot{y}_s - k_o(u_o - u_s)\sin\beta_o\cos\beta_o\sin\varphi - k_o(y_o - y_s)\sin^2\beta_o\sin\varphi + k_{sy}y_s = 0 \\ M_o\ddot{u}_o + k_o(u_o - u_s)\cos^2\beta_o + k_o(y_o - y_s)\sin\beta_o\cos\beta_o = T_o/R_o \\ m_o\ddot{y}_o + k_o(u_o - u_s)\sin\beta_o\cos\beta_o + k_o(y_o - y_s)\sin^2\beta_o + k_{oy}y_o = 0 \end{cases} \tag{8}$$

2.1.3. Overall System

By combining Equations (5) and (8), we obtain the differential equations of the FMMGIA system in the matrix form, which can be expressed as

$$\boldsymbol{m}\ddot{\boldsymbol{x}} + \boldsymbol{k}\ddot{\boldsymbol{x}} = \boldsymbol{F} \tag{9}$$

where **m** is the mass matrix, **k** is the stiffness matrix, and **F** is load vector matrix, individually defined as follows:

$$\begin{aligned} \boldsymbol{m} &= \mathrm{diag}\left(\begin{bmatrix} M_I & m_I & M_s & m_s & M_o & m_o \end{bmatrix}\right) \\ \boldsymbol{F} &= \begin{bmatrix} T_I/R_I & 0 & 0 & 0 & T_o/R_o & 0 \end{bmatrix} \end{aligned}$$

$$\boldsymbol{k} = \begin{bmatrix} k_I\cos^2\beta_I & k_I\sin\beta_I\cos\beta_I & -k_I\cos^2\beta_I & -k_I\sin\beta_I\cos\beta_I & 0 & 0 \\ k_I\sin\beta_I\cos\beta_I & k_I\sin^2\beta_I + k_{Iy} & -k_I\sin\beta_I\cos\beta_I & -k_I\sin^2\beta_I & 0 & 0 \\ -k_I\cos^2\beta_I\csc\varphi & -k_I\sin\beta_I\cos\beta_I\csc\varphi & k_o\cos^2\beta_o\csc\varphi + k_s + k_I\cos^2\beta_I\csc\varphi & (k_I\sin\beta_I\cos\beta_I + k_o\sin\beta_o\cos\beta_o)\csc\varphi & -k_o\cos^2\beta_o & -k_o\sin\beta_o\cos\beta_o \\ -k_I\sin\beta_I\cos\beta_I\sin\varphi & -k_I\sin^2\beta_I\sin\varphi & (k_I\sin\beta_I\cos\beta_I + k_o\sin\beta_o\cos\beta_o)\sin\varphi & k_I\sin^2\beta_I\sin\varphi + k_{sy} + k_o\sin^2\beta_o\sin\varphi & -k_o\sin\beta_o\cos\beta_o\sin\varphi & -k_o\sin^2\beta_o\sin\varphi \\ 0 & 0 & -k_o\cos^2\beta_o & -k_o\sin\beta_o\cos\beta_o & k_o\cos^2\beta_o & k_o\sin\beta_o\cos\beta_o \\ 0 & 0 & -k_o\sin\beta_o\cos\beta_o & -k_o\sin^2\beta_o & k_0\sin\beta_o\cos\beta_o & k_o\sin^2\beta_o + k_{oy} \end{bmatrix}$$

2.1.4. Magnetic Coupling Stiffness Calculation

Table 1 lists the parameters of the example FMMGIA system. A three-dimensional finite element model was built for the magnetic gear. In this model, the back iron materials of the input and output rotors were set to Q235 steel and 23TW250 silicon steel sheets, the FP material to 23TW250 silicon steel sheets, and the material of the gap between the input/output rotor and the FP to air. There were a total of 10 silicon steel sheets in the back iron, each with a thickness of 0.5 mm. Upon initiating the magnetic gear system, the input rotor, output rotor, and FP were all stationary, and the relative positions between the input/output rotor and the end-face of the FP at that instant were set as the initial position.

Table 1. Parameters of the linear field modulated magnetic gear with intersecting axes.

Name of parameter	Value	Name of parameter	Value
Number of pole pairs of the PMs on the input rotor p_1	4	Number of pole pairs of the PMs on the output rotor p_2	17
Number of magnetic stripes of the FP	21	Internal radius of PMs of the input/output rotors R_1 (mm)	110
External radius of the PMs of the input/output rotors R_2 (mm)	125	Axial thickness of the PMs of the input/output rotors h_m (mm)	10
Thickness of the Q235 back iron of the input/output rotors (mm)	15	Thickness of the air gaps at the input/output rotors h_a (mm)	1
Thickness of the silicon steel back iron of the input/output rotors (mm)	5	Minimum axial length of the FP I_f (mm)	15
Diameter of the back iron of the input/output rotors d (mm)	250	Intersection angle between the input and output rotors (°)	90
Transmission ratio	4.25	Remanence of PMs Br/T	1.3
Coercive force of the PMs Hc/KOe	11.6		

If, for a circular area originating at the center of the air gaps of the input/output rotors and having a radius R, the radial, tangential, and axial components of its magnetic flux density are assumed to be B_{rI}, B_{tI}, B_{aI} and B_{ro}, B_{to}, B_{ao}, respectively, then the radial and tangential force densities of the magnetic stresses on the input and output rotors can be expressed as

$$\begin{cases} f_{It} = \dfrac{B_{rI}B_{tI}}{\mu_0} & f_{ot} = \dfrac{B_{ro}B_{to}}{\mu_0} \\ f_{Ir} = \dfrac{B_{rI}^2 - B_{tI}^2}{2\mu_0} & f_{or} = \dfrac{B_{ro}^2 - B_{to}^2}{2\mu_0} \end{cases} \tag{10}$$

where μ_0 is the permeability of vacuum.

Subsequently, by selecting the integration path as the same area that originates at the center of the lateral air gaps and has a radius of R, the magnetic coupling stiffnesses between the input/output rotor and the FP can be derived based on the radial and tangential magnetic pulls on the input and output rotors, as given below:

$$\begin{cases} k_{It} = \int_{R_1}^{R_2}\displaystyle\int_0^{2\pi} \frac{R}{\mu_0}\frac{\partial\left(B_{rI}B_{tI}\right)}{\partial u_I}\mathrm{d}\theta_I\mathrm{d}R = \int_{R_1}^{R_2}\int_0^{2\pi} \frac{R}{\mu_0}\frac{\partial\left(B_{rI}B_{tI}\right)}{R\partial\theta_I}\mathrm{d}\theta_I\mathrm{d}R \\ k_{ot} = \displaystyle\int_{R_1}^{R_2}\int_0^{2\pi} \frac{R}{\mu_0}\frac{\partial\left(B_{ro}B_{to}\right)}{\partial u_o}\mathrm{d}\theta_o\mathrm{d}R = \int_{R_1}^{R_2}\int_0^{2\pi} \frac{R}{\mu_0}\frac{\partial\left(B_{ro}B_{to}\right)}{R\partial\theta_o}\mathrm{d}\theta_o\mathrm{d}R \\ k_{Ir} = \displaystyle\int_{R_1}^{R_2}\int_0^{2\pi} \frac{R}{2\mu_0}\frac{\partial\left(B_{rI}^2 - B_{tI}^2\right)}{\partial u_I}\mathrm{d}\theta_I\mathrm{d}R = \int_{R_1}^{R_2}\int_0^{2\pi} \frac{R}{2\mu_0}\frac{\partial\left(B_{rI}^2 - B_{tI}^2\right)}{R\partial\theta_I}\mathrm{d}\theta_I\mathrm{d}R \\ k_{or} = \displaystyle\int_{R_1}^{R_2}\int_0^{2\pi} \frac{R}{2\mu_0}\frac{\partial\left(B_{ro}^2 - B_{to}^2\right)}{\partial u_o}\mathrm{d}\theta_o\mathrm{d}R = \int_{R_1}^{R_2}\int_0^{2\pi} \frac{R}{2\mu_0}\frac{\partial\left(B_{ro}^2 - B_{to}^2\right)}{R\partial\theta_o}\mathrm{d}\theta_o\mathrm{d}R \end{cases} \tag{11}$$

Next, by selecting circular areas which originate at the center of the air gaps but have different radii ($R_1 \leqslant R \leqslant R_2$), we can derive the axial, tangential and radial magnetic flux densities of the different radii R, R_1, and R_2 through finite element simulation, as shown in Fig. 3. It can be seen that although the arc length of the PM's location varies with different radii, because the PMs all share the same size, material and fan shape, and are layered at regular intervals, the axial and tangential magnetic flux densities of different radii are almost identical, whilst the radial magnetic flux densities differ only slightly.

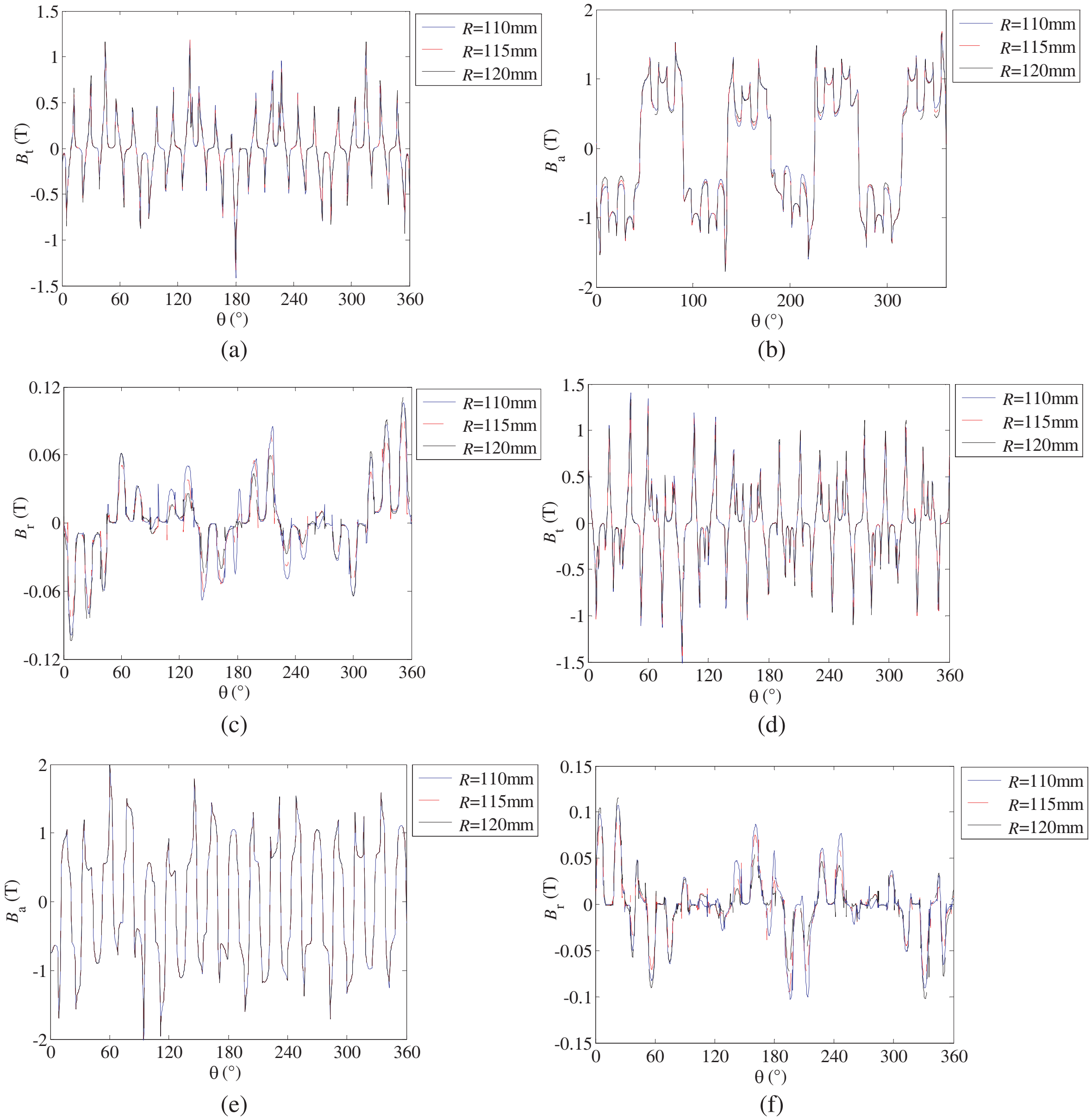

(a) (b) (c) (d) (e) (f)

Figure 3. Magnetic flux densities under different radii: (a) Air gaps near the input rotor; (b) Air gaps near the input rotor; (c) Air gaps near the input rotor; (d) Air gaps near the output rotor; (e) Air gaps near the output rotor; (f) Air gaps near the output rotor.

If we ignore subtle differences in the magnetic flux distribution at the middle of the air gaps, the magnetic coupling stiffnesses between the input/output rotor and the FP can be expressed as

$$\begin{cases} k_{It} = \displaystyle\int_0^{2\pi} \frac{(R_2 - R_1)}{\mu_0} \frac{\partial\left(B_{rI}B_{tI}\right)}{\partial\theta_I} \mathrm{d}\theta_I \\ k_{ot} = \displaystyle\int_0^{2\pi} \frac{(R_2 - R_1)}{\mu_0} \frac{\partial\left(B_{ro}Bt_{ao}\right)}{\partial\theta_o} \mathrm{d}\theta_o \\ k_{Ir} = \displaystyle\int_0^{2\pi} \frac{(R_2 - R_1)}{2\mu_0} \frac{\partial\left(B_{rI}^2 - B_{tI}^2\right)}{\partial\theta_I} \mathrm{d}\theta_I \\ k_{or} = \displaystyle\int_0^{2\pi} \frac{(R_2 - R_1)}{2\mu_0} \frac{\partial\left(B_{ro}^2 - B_{to}^2\right)}{\partial\theta_o} \mathrm{d}\theta_o \end{cases} \tag{12}$$

For a stationary input rotor, the magnetic coupling stiffness curves of the components in the FMMGIA system when the output rotor rotates to different angles relative to the initial position are shown in Fig. 4.

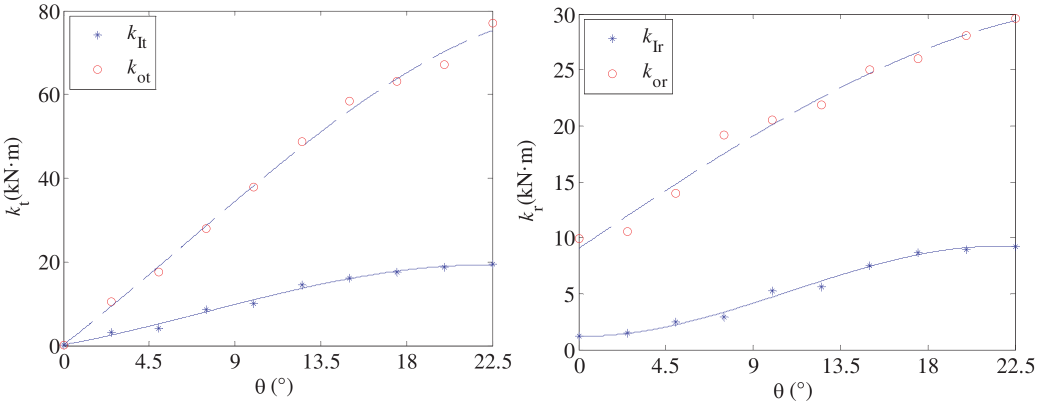

Figure 4. Magnetic coupling stiffness curves of the magnetic gear.

It can be seen from Fig. 4 that the magnetic coupling stiffnesses between the input/output rotor and the FP change with the rotational angle of the output rotor. Specifically, when the rotational angle is 0° — that is, when the output torque of the magnetic gear is 0 N·m — the tangential magnetic coupling stiffness is zero. On the contrary, when the rotational angle is 22.5°, that is, the output torque of the FMMGIA is the largest, the tangential magnetic coupling stiffness reaches its maximum. Therefore, the tangential magnetic coupling stiffness increases with increasing output load. Similarly, the radial magnetic coupling stiffness also increases with the rotational angle of the output rotor, or the output torque; however, the initial radial stiffness is never zero, which indicates the constant presence of an unbalanced radial magnetic pull. Furthermore, the radial and tangential magnetic coupling stiffnesses between the output rotor and the FP are consistently larger than those between the input rotor and FP, and both values are considerably smaller than the meshing stiffness of the mechanical gear at 2–3 orders of magnitude [17].

3. MODAL ANALYSIS OF THE FMMGIA SYSTEM

Table 2 shows the corresponding stiffness and mass parameters of the example system shown in Table 1 when is at maximum load.

Table 2. Stiffness and mass parameters of the fully loaded example magnetic gear system.

M_I/M_o (kg)	m_I/m_o (kg)	M_s (kg)	m_s (kg)	k_{It} (N/m)	k_{Ir} (N/m)
5.92	10.72	2.91	7.45	1.9823×10^4	9.2130×10^3
k_{ot} (N/m)	k_{or} (N/m)	k_{Iy} (N/m)	k_{oy} (N/m)	k_{sy} (N/m)	k_s (N/m)
7.1363×10^4	2.9631×10^4	1.5×10^7	1.5×10^7	1.7×10^7	1.0×10^7

The modal frequency of each order and the corresponding modal shapes of the FMMGIA system can be derived by substituting the parameters in Table 2 into differential Equation (9) and ignoring the external load fluctuation. The results are shown in Table 3.

An analysis of the characteristics of the modal frequencies and shapes suggests that the transmission system of the FMMGIA has the following features:

(1) The FMMGIA system has 6 orders modal. Among them, two order modalds have smaller frequencies, while the rest have substantially larger frequencies. For different orders modal, while

Table 3. Modal frequencies and corresponding modal shapes of the FMMGIA system.

	IRTM	IRLM	FPTM	FPLM	ORTM	ORLM
Frequency (rad/s)	55.0	1183.1	1864.8	1513.6	105.1	1183.3
Modal shapes	1.0000	−0.0010	−0.0009	0.0006	0.0029	−0.0000
	−0.0006	−1.0000	−0.0004	0.0004	−0.0000	−0.0064
	0.0025	−0.0020	1.0000	0.0147	−0.0065	0.0045
	0.0007	−0.0008	0.0057	−1.0000	−0.0023	0.0024
	0.0039	−0.0000	−0.0032	0.0020	−1.0000	0.0033
	−0.0000	−0.0085	−0.0012	0.0012	0.0018	1.0000

the vibration displacement is relatively large at one degree of freedom, it is significantly smaller at all the other degrees of freedom, indicating a weak coupling between different degrees of freedom. This is because different components are connected by magnetic coupling, and therefore, the torsional magnetic coupling stiffnesses between the input/output rotors and the FP are substantially smaller than the lateral support stiffnesses of the input/output rotors and the torsional and lateral support stiffnesses of the FP. According to the characteristics of the modal shapes corresponding to different modal frequencies, we have named each modal as the torsional or the lateral modal of the input rotor, FP, and output rotor (IRTM, IRLM, FPTM, FPLM, ORTM, and ORLM).

(2) Because of their structural similarity, the input and output rotors of the FMMGIA system have identical physical masses as well as equivalent masses when rotating around the axis. However, as the tangential magnetic coupling stiffness between the output rotor and FP increases, the corresponding inherent frequency of the ORTM also increases. Changing the number of PM pole pairs of the input and output rotors can change the input/output torque ratio, which in turn alters the magnetic coupling stiffnesses between the input/output rotors and FP and thus, the natural frequencies.

(3) As the input and output rotors adopt the same support mode and material, their torsional and lateral support stiffnesses are fundamentally consistent. However, different lateral magnetic coupling stiffnesses between the components and identical masses of the input and output rotors result in approximately similar lateral vibration frequencies between the input and output rotors.

4. EFFECTS OF PRIMARY DESIGN PARAMETERS ON THE NATURAL FREQUENCY OF THE FMMGIA SYSTEM

The modal frequency of the FMMGIA system is of great significance to its dynamic characteristics. Investigation into the effects of the primary design parameters on the modal frequency of the FMMGIA system can provide references to optimize its design as well as to enhance its stability.

As shown in Fig. 5(a), when the masses of the back irons of the input and output rotors gradually increase, their lateral modal frequencies decrease sharply, whilst their torsional modal frequencies decrease slowly. However, both the torsional and lateral modal frequencies of the FP remain almost unchanged. This is because with the simultaneous increase of m_I and m_o, the equivalent masses of the two rotors along the rotational direction increase, but the magnetic flux densities of the air gaps are scarcely influenced at the same time. Therefore, only the magnetic coupling stiffness increases slowly.

As shown in Fig. 5(b), as the remanence of the PMs gradually increases, the magnetic coupling stiffnesses between the input/output rotor and the FP increase. More specifically, the torsional magnetic coupling stiffnesses between the input/output rotor and FP increase to a larger extent than the lateral magnetic coupling stiffnesses. Therefore, the modal frequencies of the torsional modes of the input rotor, output rotor, and FP increase accordingly, whereas the lateral modal frequencies do not change significantly.

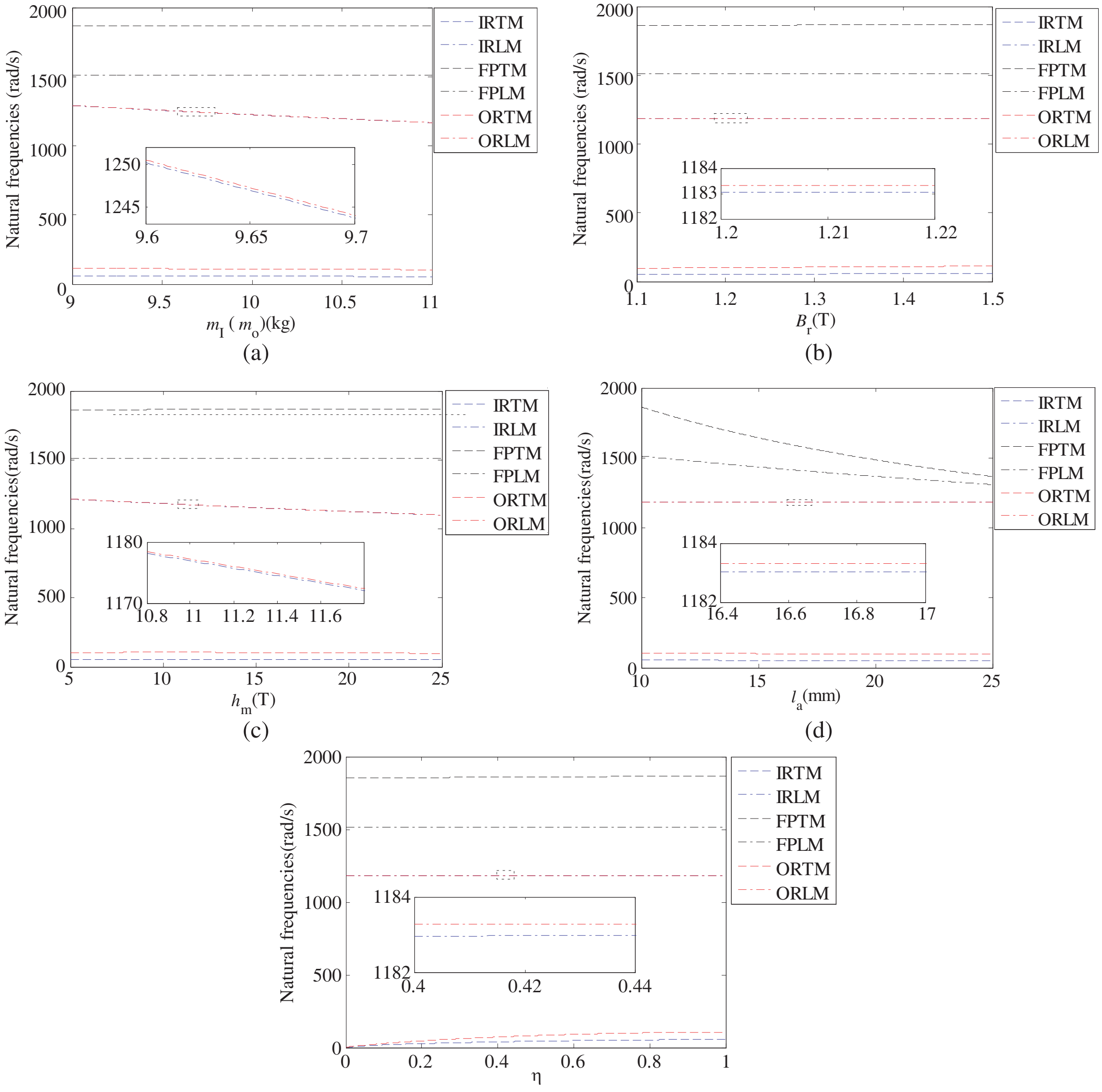

(a) (b) (c) (d) (e)

Figure 5. Effects of primary design parameters on natural frequency: (a) m_I/m_o; (b)B_r; (c) h_m; (d)l_a; (e) η.

As the PM thickness increases, the magnetic flux densities of the air gaps increase correspondingly. Simultaneously, the maximum static output torque of the magnetic gear system is escalated, which in turn increases the magnetic coupling stiffnesses between the input/output rotor and FP. However, after the thicknesses of the PMs reach a certain value, increase in the magnetostatic energy is compensated by the magnetoresistance loss. Consequently, the increase in the maximum static output torque of the FMMGIA and the magnetic coupling stiffnesses between different components almost halts despite the constantly growing volume of the PMs. Therefore, as shown in Fig. 5(c), the modal frequencies of the torsional modes of the input and out rotors in the magnetic gear system first increase, then decrease, while the modal frequency of the torsional modal of the FP tends to stabilize after a certain period of growth.

As shown in Fig. 5(d), when the minimum axial length of the FP increases, besides a rapid increase in the masses of the FP, the magnetoresistance also escalates, which leads to a decreased maximum static torque of the magnetic gear system as well as reduced magnetic coupling stiffnesses between components. Consequently, each order of modal frequency decreases. Among all the modal frequencies, the frequencies of the torsional and lateral modals of the FP demonstrate the most significant reduction, followed by those of the torsional vibration modes of the input and output rotors. On the contrary, the modal frequencies of the lateral modal of the two rotors do not change significantly.

If the ratio between the current output load and the maximum output load of the FMMGIA system is defined as the load factor η, then the tangential and radial magnetic coupling stiffnesses between different components increase with increasing η. Out of these, increase in the tangential magnetic coupling stiffness is the most obvious, contributing to considerable increases in various torsional modal frequencies, as shown in Fig. 5(e). On the contrary, as increase in the lateral magnetic coupling stiffness is negligible compared to the lateral support stiffness, the modal frequencies of the various lateral modals remain almost unchanged.

5. MODAL EXPERIMENT OF THE EXAMPLE FMMGIA SYSTEM

Experimental verification of the modal of the magnetic gear system is of great importance for validating the established dynamic model. In this study, we adopted the hammering method to measure the modal frequencies of the example magnetic gear system. A prototype of the example system described in Table 1 is shown in Fig. 6; it consisted of a driving motor, the magnetic gear prototype, a magnetic powder loader, and a hammering vibration measurement system. A wireless torque sensor was installed between the output shaft of the FMMGIA and the magnetic powder loader to display the output torque in real time by transferring the data to the computer program via a wireless torque receiver. The magnetic powder loader was used to apply a fixed load to the output shaft exceeding the maximum output torque for the magnetic gear system. A frequency-transducer was used to adjust the rotational speed of the three-phase AC motor to 100 r/min. The magnetic gear system was discontinuously started several times by motor, after which braking was performed by the voltage reversal braking until the intersection angle between the input and output shafts approached 22.5°, so that the system could operate at approximately the maximum output load. Subsequently, the modal frequencies of the components at different degrees of freedom were measured using the multi-point excitation and single-point response method; the measurement results are listed in Table 4.

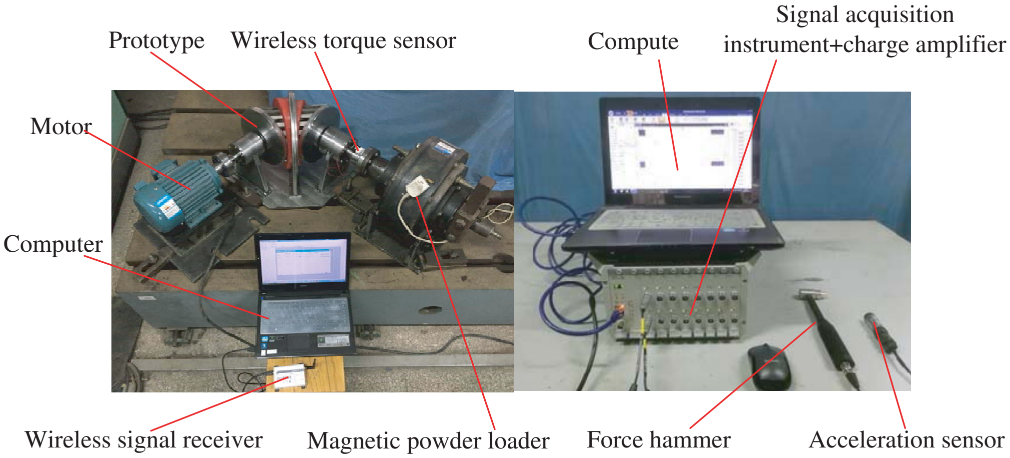

Figure 6. Modal experiment platform for the example magnetic gear system.

Table 4 clearly displays a good agreement between the measured and theoretically predicted modal frequencies, thereby validating the dynamic model of a magnetic gear system. However, there are still discrepancies between the experimental and theoretical results, the largest of which can be observed in the frequencies corresponding to the torsional vibration modals of the input and output rotors. These can be explained as follows:

(1) The theoretical predication of the torsional modal frequencies of both the input and output rotors are higher than the measured values. This is mainly because the magnetic coupling stiffnesses

Table 4. Measured modal frequencies and errors.

Modal	IRTM	IRLM	FPTM	FPLM	ORTM	ORLM
Theoretical value (rad/s)	55.0	1183.1	1864.8	1513.6	105.1	1183.3
Measured value (rad/s)	53.2	1325.6	1786.9	1687.3	102.5	1353.6
Error (%)	17.39	12.05	4.43	11.49	19.48	14.39

between different components are derived based on the finite element method, whereas factors such as the magnetic flux leakage of the components, magnetoresistance loss, incomplete magnetizing of the PMs, and structural inhomogeneity of the material are not considered, thereby leading to higher theoretically predicted values of magnetic coupling stiffnesses.

(2) The magnetic coupling stiffness between different components of the FMMGIA is not always linear, which introduces errors between theoretical calculations and experimental measurements.

(3) The lateral support stiffness of each component is derived from finite element simulation, which differs from that of the actual structure, thereby introducing errors.

(4) In this study, we used a motor to set the intersectional angle between the input and output rotors of the example magnetic gear system to 22.5°. However, as the inertia of the magnetic power loader was significant, in the actual measurements, the intersection angle was not exactly 22.5°.

6. CONCLUSION

In this study, we developed a three-dimensional dynamic FMMGIA model and corresponding differential equations, analyzed the modal characteristics of the system, and identified the effects of different design parameters on the modal frequency. It was found that the weak magnetic coupling stiffnesses between different components of the FMMGIA vary with the output torque, which relies on the relative intersection angle between the input and output rotors, and the maximum magnetic coupling stiffnesses are reached when the output torque is the largest. It is seen that the FMMGIA can be divided into 6 orders modals based on their characteristics, including the torsional and lateral modals of the input rotor, FP, and output rotor. Although the coupling of all modals between different degrees of freedom was found relatively weak, the torsional modal frequencies of the input and output rotors are the lowest and are more easily affected by design parameters such as the remanence of the PMs.

The lower natural frequencies caused by the weak magnetic coupling stiffnesses between different components will be easy to result in the low frequency resonances of the FMMGIA system. These will slowly decay and deteriorate dynamic behavior of the FMMGIA system. In order to enhance the service performance and consider the nonlinear of the magnetic coupling stiffness, it will be necessary to study the nonlinear dynamic characteristics and vibration control of the FMMGIA system.

ACKNOWLEDGMENT

This project is supported by the National Natural Science Foundation of China (grant No. 51675463) and the Natural Science Foundation of Hebei Province of China (E2017203098). We would like to thank Editage (www.editage.cn) for English language editing.

REFERENCES

1. Jian, L. and K.-T. Chau, "Analytical calculation of magnetic field distribution in coaxial magnetic gears," *Progress In Electromagnetics Research*, Vol. 92, 1–16, 2009.
2. Rasmussen, P. O., T. O. Andersen, F. T. Jorgensen, and O. Nielsen, "Development of a high performance magnetic gear," *IEEE Transactions on Industry Applications*, Vol. 41, No. 3, 764–770, 2005.

3. Percebon, L. A., R. Ferraz, D. L. Ferreira, and V. Mauricio, "Modelling of a magnetic gear considering rotor eccentricity," *IEEE International Electric Machines and Drives Conference (IEMDC)*, 2011.
4. Liu, C. and K. T. Chau, "Electromagnetic design of a new electrically controlled magnetic variable-speed gearing machine r," *Energies*, No. 7, 1539–1554, 2014.
5. Iwasaki, N., M. Kitamura, and Y. Enomoto, "Optimal design of permanent magnet motor with magnetic gear and prototype verification," *Electrical Engineering in Japan*, Vol. 194, No. 1, 60–69, 2016.
6. Mezani, S., K. Atallah, and D. Howe, "A high-performance axial-field magnetic gear," *Journal of Applied Physics*, Vol. 99, No. 8, R303, 2006.
7. Du, S., J. Jiang, Y. Zhang, and Y. Gong, "A magnetic gearing," *Transactions of China Electrotechnical Society*, Vol. 25, No. 9, 41–46, 2010.
8. Jian, L., G. Xu, J. Song, H. Xue, D. Zhao, and J. Liang, "Optimum design for improving modulating-effect of coaxial magnetic gear using response surface methodology and genetic algorithm," *Progress In Electromagnetics Research*, Vol. 116, 297–312, 2011.
9. Uppalapati, K. K. and J. Z. Bird, "An iterative magnetomechanical deflection model for a magnetic gear," *IEEE Transactions on Magnetics*, Vol. 50, No. 2, 7005904, 2014.
10. Hao, X. H., X. J. Zhu, and H. Zhang, "Free vibration of the electromechanical integrated magnetic gear system," *Journal of Vibroengineering*, Vol. 17, No. 3, 1120–1132, 2015.
11. Frank, N. W., S. Pakdelian, and H. A. Toliyat, "Passive suppression of transient oscillations in the concentric planetary magnetic gear," *IEEE Transactions on Energy Conversion*, Vol. 26, No. 3, 933–939, 2011.
12. Montague, R., C. Bingham, and K. Atallah, "Servo control of magnetic gears," *IEEE/ASME Transactions on Mechatronics*, Vol. 17, No. 2, 269–278, 2012.
13. Liu, X., Y. Y. Zhao, S. D. Huang, M. Lu, and Y. D. Chen, "Investigation of the transient and vibration characteristics of a dual-flux-modulator coaxial magnetic gear," *Diangong Jishu Xuebao*, Vol. 34, No. 9, 1865–1874, 2019.
14. Wang, Z., J. Chen, M. Cheng, and K. T. Chau, "Field-oriented control and direct torque control for paralleled VSIs fed PMSM drives with variable switching frequencies," *IEEE Transactions on Power Electronics*, Vol. 31, No. 3, 2417–2418, 2016.
15. Liu, Y., S. L. Ho, and W. N. Fu, "A novel magnetic gear with intersecting axes," *IEEE Transactions on Magnetics*, Vol. 50, No. 11, 8001804, 2014.
16. Hao, X., H. Q. Zhu, X. M. Guan, and D. Pan, "Magnetic gear with intersecting axes and straight stationary pole-pieces," *Advances in Mechanical Engineering*, Vol. 10, No. 11, 1–10, 2018.
17. Zhang, L., Y. Wang, K. Wu, R. Y. Sheng, and Q. L. Huang, "Dynamic modeling and vibration characteristics of a two-stage closed-form planetary gear train," *Mechanism and Machine Theory*, Vol. 97, 12–28, 2016.